Space Mission Analysis and Design, 3rd Edition
Errata as of January 29, 2003

The following errata are provided to keep this volume as useful as possible. We would appreciate any other corrections or suggestions being reported to:

Donna Klungle, Microcosm, Inc.,
401 Coral Circle, El Segundo, CA 90245-4622
Phone: (310) 726-4100, Fax: (310) 726-4110
e-mail to: bookproject@smad.com.

The editors of SMAD apologize to Dr. Robert K. McMordie for not listing him as an author of Section 11.5 in the first through third printings of SMAD III. The text of Section 11.5 in the 4th printing includes corrections which were identified by Dr. McMordie, for which we are grateful.

ERRATA

PAGE	THIRD EDITION, FIRST PRINTING
136	In Eq. (6-9), " ^{2}" should be " V^2"
143	In Eq. (6-20), "1.032.37" should be "1.032 37"
144	In the caption of Table 6-4, "precursor" should be "precession"
	In Table 6-4, the row for $\dot{\omega}$ for the Shuttle, "0.002 42" should be "0.000 31" and "0.001 10" should be "0.000 14"
177	In Fig. 7-8, the F10.7 and Ap labels are reversed from top to bottom, i.e., F10.7 = 225, Ap = 20 is the top line, F10.7=175, Ap = 16 is the second line, etc. Also, in the caption, "Ballistic Coefficient of 65 kg/m^2" should be "Ballistic Coefficient of 100 kg/m^2"
192	On Fig. 7-10, "S/2" is half the distance between the centers of the two coverage circles.
192	On Fig. 7-11, the spacing between the two orbits is D_{maxS}.
198	In Table 7-12, Step 6, "Table 7-14" should be "Table 7-13" in both columns.
209	Fig. 8-2 has been corrected. The revised figure appears in the pages following the errata listing.
218	On Fig. 8-11, "1–8" should be "1–8 Å"
234	Last paragraph, 3rd line: "Sec. 8.1.4" should read "Sec. 8.1.5".
242	1st partial paragraph, 6th line: "NASA Earth Observing System" should read "Terra spacecraft in NASA Earth Observing System".
255	In Fig. 9-4, in the Visible, Ultraviolet, and Infrared regions of the spectrum, the wavelength units should be "μm," not "m". X-Rays sample mission "AXAF" should read "Chandra".
264	The expression in the fifth line following Eq. (9-10) should be "1/sin ε," not "1/cos ε."
265	In Table 9-9, in the Visible column of the top row, "0.366" should be "0.366 m".
286–287	Last paragraph on page 286 and text above Table 9-15 on page 287 have been rewritten. Corrected pages appear following the errata listing.
294	In Eq. (9-31), "10-5" should read "10^{-5}".
297	1st paragraph in Sec. 9.6.2, 3rd line: "EOS" should read "Terra".
298	1st paragraph, 1st and 4th lines: "EOS" and "EOS AM" should read "Terra".
428	In Fig. 11-14, the three minus signs in the labels should all be plus-or-minus signs (i.e., $1,367 \pm 5$ W/m^2, Albedo 30 ± 5 %, 237 ± 21 W/m^2).
449	In Table 11-48: Source for row 9 thru 12 should read "Fig. 11-14" not "Fig. 11-18". Symbol for row 19 should read "A_R" not "A_r," and Symbol for row 20 should read "T_R" not "T_r".
456	In Sec. 11.5.7: "Design Temperature Range" section has been rewritten. Corrected page appears following the errata listing.

548	In Sec. 13.2.2: • 1st paragraph, last line: "Sec. 9.1" should read "Sec. 9.5.5" • 2nd paragraph, 3rd line: replace "From Eq. (9-35)" with "Here" • 3rd paragraph, 1st line: "Eq. (9-34)" should read "Eq. (9-23)" • 3rd paragraph, 2nd line: "11 Gbps" should read "85 Mbps" • 3rd paragraph, 3rd line: "1 m^2" should read "30 m" • 3rd paragraph, 6th line: "2.5 million pixels" should read "2,900 pixels" and "8.5 Mbps" should read "39 kbps"
549	Continuing in Sec. 13.2.2: • 1st line: "2 bits" should read "8 bits" • In Table 13-7, Parameter column: "Scan width (km)" should read "SW = Scan width (km)" • In Table 13-7, FireSat column should read: 700; 6,800; 30; 2,700; 57.9; Continuous; 145 µs/scan width; 1.6; 8; 0.95; 85 x 10^6 • Footnote equation should read: $\left((25 \times 25)\ \text{km}^2 \right) \left(\frac{10^3\,\text{m}}{\text{km}} \right)^2 \left(\frac{1\ \text{pixel}}{30\ \text{m}} \right)^2 \left(\frac{1}{4\ \text{min}} \right) \left(\frac{4\ \text{min}}{60\ \text{sec}} \right)$
554	In Eqs. (13-13) and (13-14): delete L_{pt} term. Because Table 13-13 sets $G_t = G_{pt} + L_{pt}$, L_{pt} is counted twice in the equations. Also delete L_{pt} in listing of variables that appears in text between the two equations.
555	3rd paragraph: "$C/N_0 - \log B$" should read "$C/N_0 B$ or, in dB, is $C/N_0 - 10 \log B$". Also "Eq. (13-15a)" should read "Eq. (13-15b)"
557	Fig. 13-7 has been revised. See corrected page appears following the errata listing.
566	In Table 13-12, the asterisk corresponding to the footnote should be in the rightmost column (Downlink Power) of the X-band row. The value in that cell should be "–142/4 kHz*". Also Downlink Power Ku value should read "12.5–12.75" not "12.5–2.75".
567	Table 13-13 has been revised. See corrected page appears following the errata listing.
584	In Fig. 13-20: "50 W @ 60 GHz" (top right corner) should read "5 W @ 60 GHz"
677	In Table 16-20, top row: All "V_n" should read "V_g"
703	Table 17-9 has been revise. See corrected page appears following the errata listing.
843	Fig. 21-3-7 has been revised. See corrected page appears following the errata listing.
899	In Fig. B-1: second "ϕ'" from origin should read "ϕ"
900	In Eq. (B-7), "$\tan^{-1}(Y/Z)$" should be "$\tan^{-1}(Y/X)$."
903	• "Specific angular momentum" section, 1st paragraph: "h, r, and V" are vectors and should appear in bold type • "True anomaly" section, last equation: radical sign should not extend over tan.
908-913	Appendix E has been both corrected and revised to improve clarity. The revised appendix is contained in the following pages.

PAGE	THIRD EDITION, SECOND PRINTING
97	In Fig. 5-1C: Put arrowhead on other end of "Roll Rotation"
110	1st full paragraph: both references to Eq. (5-13b) should be to Eq. (5-13c).
110	Eq. (5-15) should read: $F = F_0 (1 - \Phi / 360 \text{ deg})$
110	5th full paragraph, 9th line: "If $\Phi > \Phi_{90}$," should read "If $\Phi /2$ the larger of $\lvert Az_N \pm \Phi_{90}\rvert$,"
327	In Table 10-20 • "Reaction Wheels" row, "Weight" column: "2 1 0.4 x H" should read "2 + 0.4 x H" and "5 1 0.1 x H" should read "5 + 0.1 x H" • "Control Moment Gyros" row, "Weight" column: "4 1 0.03 x T" should read "4 + 0.03 x H"
577	In Fig. 13-16: Added axes labels in "Time" and "Frequency" columns. See corrected table that follows the errata listing.
790	In 3rd full paragraph, 2nd line: "Herzberg" should be "Hertzfeld"
818	Last reference entry: "Herzberg" should be "Hertzfeld"
899	In Fig. B-1: for notation consistency change "b" to "c"
901	1st line of text: "$\phi' = \sin^{-1} Z$" should read "$\phi' = \sin^{-1} (Z /r)$"
Inside Rear Cover	In "Explanation of Earth Satellite Parameters," entry for Col. 41: 1st exponent should not be negative.

| PAGE	THIRD EDITION, THIRD PRINTING
112–114	These pages have been revised to improve clarity. The revised pages follow the errata listing.
115	In Fig. 5-15B: The celestial equator is 10 degrees too high.
186	In Table 7-9, last entry, 4th column: Reference should read "Eq. (6-37)" not "Eq. (6-33)".
411	3rd paragraph, 3rd line: "(260 kg)" should read "(118 kg)".
435	2nd paragraph: <u>SHOULD READ</u> "For heat transfer between two bodies we generally assume diffuse gray surface conditions (*diffuse* means that the reflected and emitted radiation follow Lambert's cosine law and the *gray* surfaces are those for which emissivity and absorptivity are independent of wavelength)."
435	5th paragraph including Eq. (11-17) should be deleted.
435	Paragraph before Eq. (11-18): <u>SHOULD READ</u> "For two flat surfaces at a very small distance apart we use:"
436	Paragraph following Eq. (11-19): <u>SHOULD READ</u> "For the equations given above σ is the Stefan-Boltzmann constant, *A* is area in m^2, ε is emissivity, and *T* is temperature in degrees K. Note that in Eq. (11-19) the subscript 1 refers to the inside surface and 2 to the outside surface."
440	Paragraph following Fig. 11-20, 1st sentence: <u>SHOULD READ</u> "The heat pipe shown in Fig. 11-20 is a *fixed conductance heat pipe.*"
444	Replace 2nd sentence of "Thermal Mathematical Model (TMM) with "The nodes represent physical locations on the spacecraft and are connected to each other by thermal conductors. If the model is for transient analyses, thermal capacitors are attached to the node points."
444	Sentence just before Fig. 11-21: insert "and" before "ESTAN".
446	1st sentence following Eq. (11-30): <u>SHOULD READ</u> "For a solar array, the energy balance equation includes a power generation term since the solar cells convert solar energy directly to electrical energy."
448	In 5th definition, solar array efficiency: Replace "÷" with "to".
449	1st line following Eq. (11-36): <u>SHOULD READ</u> "where *Q* is the input (or output) energy per unit time in W, . . ."
669	Table 16-17 has been updated. See updated table in pages following the errata listing
847	In Fig. 21.4: Units added to axes labels, i.e., "Penetrating Projectile Diameter (cm)" and "Impact velocity (km/s)".

We wish to find the angular relationships between a target, **P**, on the surface of the Earth, and a spacecraft with subsatellite point, *SSP*, also on the surface of the Earth, as shown in Fig. 5-12. We assume that the subsatellite point's latitude, Lat_{SSP} and longitude, $Long_{SSP}$, are known. Depending on the application, we wish to solve one of two problems: (1) given the coordinates of a target on the Earth, find its coordinates viewed by the spacecraft, or (2) given the coordinates of a direction relative to the spacecraft, find the coordinates of the intercept on the surface of the Earth. In both cases, we determine the relative angles between *SSP* and **P** on the Earth's surface and then transform these angles into spacecraft coordinates.

Given the coordinates of the subsatellite point $(Long_{SSP}, Lat_{SSP})$ and target $(Long_P, Lat_P)$, and defining $\Delta L = | Long_{SSP} - Long_P |$, we wish to find the azimuth, Φ_E, measured eastward from north, and angular distance, λ, from the subsatellite point to the target. (See Fig. 5-12.) These are given by

$$\cos \lambda = \sin Lat_{SSP} \sin Lat_P + \cos Lat_{SSP} \cos Lat_P \cos \Delta L \quad (\lambda < 180 \text{ deg}) \qquad (5\text{-}19)$$

$$\cos \Phi_E = (\sin Lat_P - \cos \lambda \sin Lat_{SSP})/(\sin \lambda \cos Lat_{SSP}) \qquad (5\text{-}20)$$

where $\Phi_E < 180$ deg if **P** is east of *SSP* and $\Phi_E > 180$ deg if **P** is west of *SSP*.
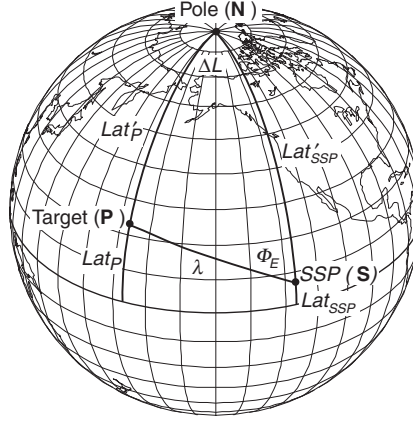
Fig. 5-12.   Relationship Between Target and Subsatellite Point on the Earth's Surface.

Alternatively, given the position of the subsatellite point $(Long_{SSP}, Lat_{SSP})$ and the position of the target relative to this point (Φ_E, λ), we want to determine the geographic coordinates of the target, $(Long_P, Lat_P)$:

$$\cos Lat_P' = \cos \lambda \sin Lat_{SSP} + \sin \lambda \cos Lat_{SSP} \cos \Phi_E \quad (Lat_P' < 180 \text{ deg}) \quad (5\text{-}21)$$

$$\cos \Delta L = (\cos \lambda - \sin Lat_{SSP} \sin Lat_P) / (\cos Lat_{SSP} \cos Lat_P) \qquad (5\text{-}22)$$

where $Lat_P' \equiv 90$ deg $- Lat_P$ and **P** is east of *SSP* if $\Phi_E < 180$ deg and west of *SSP* if $\Phi_E > 180$ deg.

We now wish to transform the coordinates on the Earth's surface to coordinates as seen from the spacecraft. By symmetry, the azimuth of the target relative to north is the same as viewed from either the spacecraft or the Earth. That is,

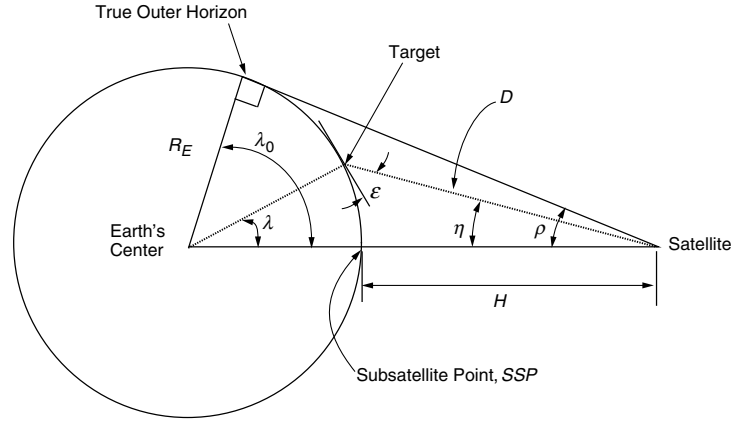$$\Phi_{E \, spc} = \Phi_{E \, surface} = \Phi_E \qquad (5\text{-}23)$$

Fig. 5-13.   Definition of Angular Relationships Between Satellite, Target, and Earth Center.

Generally, then, the only problem is to find the relationship between the *nadir angle*, η, measured at the spacecraft from the subsatellite point (= nadir) to the target; the *Earth central angle*, λ, measured at the center of the Earth from the subsatellite point to the target; and the *grazing angle* or *spacecraft elevation angle*, ε, measured at the target between the spacecraft and the local horizontal. Figure 5-13 defines these angles and related distances. First, we find the angular radius of the Earth, ρ, from

$$\sin \rho \ = \cos \lambda_0 = \ \frac{R_E}{R_E + H} \tag{5-24}$$

which is the same as Eq. (5-16). Next, if λ is known, we find η from

$$\tan \eta = \ \frac{\sin \rho \sin \lambda}{1 - \sin \rho \cos \lambda} \tag{5-25}$$

If η is known, we find ε from

$$\cos \varepsilon = \ \frac{\sin \eta}{\sin \rho} \tag{5-26a}$$

Or, if ε is known, we find η from

$$\sin \eta = \cos \varepsilon \sin \rho \tag{5-26b}$$

Finally, the remaining angle and side are obtained from

$$\eta + \lambda + \varepsilon = 90 \text{ deg} \tag{5-27}$$

$$D = R_E \ (\sin \lambda / \sin \eta) \tag{5-28}$$

Figure 5-14 summarizes the process of transforming between spacecraft coordinates and Earth coordinates.

As an example, consider a satellite at an altitude of 1,000 km. From Eq. (5-16), the angular radius of the Earth $\rho = 59.8$ deg. From Eqs. (5-17) and (5-18), the horizon is 30.2 deg in Earth central angle from the subsatellite point and is at a line-of-sight

First, compute the angular radius of Earth, ρ

$$\sin \rho = \cos \lambda_0 = R_E / (R_E + H) \tag{5-24}$$

To compute spacecraft viewing angles given the subsatellite point at ($Long_{SSP}$, Lat_{SSP}) and target at ($Long_P$, Lat_P), and $\Delta L \equiv | Long_{SSP} - Long_P |$

$$\cos \lambda = \sin Lat_{SSP} \sin Lat_P + \cos Lat_{SSP} \cos Lat_P \cos \Delta L \quad (\lambda < 180 \text{ deg}) \tag{5-19}$$

$$\cos \Phi_E = (\sin Lat_P - \cos \lambda \sin Lat_{SSP}) / (\sin \lambda \cos Lat_{SSP}) \tag{5-20}$$

$$\tan \eta = \sin \rho \sin \lambda / (1 - \sin \rho \cos \lambda) \tag{5-25}$$

To compute coordinates on the Earth given the subsatellite point at ($Long_{SSP}$, Lat_{SSP}) and target direction (Φ_E, η):

$$\cos \varepsilon = \sin \eta / \sin \rho \tag{5-26a}$$

$$\lambda = 90 \text{ deg} - \eta - \varepsilon \tag{5-27}$$

$$\cos Lat_P{}' = \cos \lambda \sin Lat_{SSP} + \sin \lambda \cos Lat_{SSP} \cos \Phi_E \quad (Lat_P{}' < 180 \text{ deg}) \tag{5-21}$$

$$\cos \Delta L = (\cos \lambda - \sin Lat_{SSP} \sin Lat_P) / (\cos Lat_{SSP} \cos Lat_P) \tag{5-22}$$

Fig. 5-14.   Summary of the Process of Transforming Between Spacecraft Viewing Angles and Earth Coordinates. Equation numbers are listed in the figure and variables are as defined in Figs. 5-11 and 5-12.

distance of 3,709 km from the satellite. We will assume a ground station at Hawaii ($Lat_P = 22$ deg, $Long_P = 200$ deg) and a subsatellite point at $Lat_{SSP} = 10$ deg, $Long_{SSP} = 185$ deg. From Eqs. (5-19) and (5-20), the ground station is a distance $\lambda = 18.7$ deg from the subsatellite point, and has an azimuth relative to north = 48.3 deg. Using Eqs. (5-25) and (5-28) to transform into spacecraft coordinates, we find that from the spacecraft the target is 56.8 deg up from nadir (η) at a line of sight distance, D, of 2,444 km. From Eq. (5-27), the elevation of the spacecraft as seen from the ground station is 14.5 deg. The substantial foreshortening at the horizon can be seen in that at $\varepsilon = 14.5$ deg we are nearly half way from the horizon to the subsatellite point ($\lambda = 18.7$ deg vs. 30.2 deg at the horizon).

Using these equations, we can construct Fig. 5-15, which shows the Earth as seen from 1,000 km over Mexico's Yucatan Peninsula in the Gulf of Mexico. The left side shows the geometry as seen on the surface of the Earth. The right side shows the geometry as seen by the spacecraft projected onto the spacecraft-centered celestial sphere. As computed above, the maximum Earth central angle will be approximately 30 deg from this altitude such that the spacecraft can see from northwestern South America to Maine on the East Coast of the U.S. and Los Angeles on the West Coast. The angular radius of the Earth as seen from the spacecraft will be 90 – 30 = 60 deg as shown in Fig. 5-15B. Because the spacecraft is over 20 North latitude, the direction to nadir in spacecraft coordinates will be 20 deg south of the celestial equator. (The direction from the spacecraft to the Earth's center is exactly opposite the direction from the Earth's center to the spacecraft.)

Even after staring at it a bit, the view from the spacecraft in Fig. 5-15B looks strange. First, recall that we are looking at the spacecraft-centered celestial sphere **from the outside**. The spacecraft is at the center of the sphere. Therefore, the view for us is reversed from right-to-left as seen by the spacecraft so that the Atlantic is on the left and the Pacific on the right. Nonetheless, there still appear to be distortions in the view. Mexico has an odd shape and South America has almost disappeared. All of this
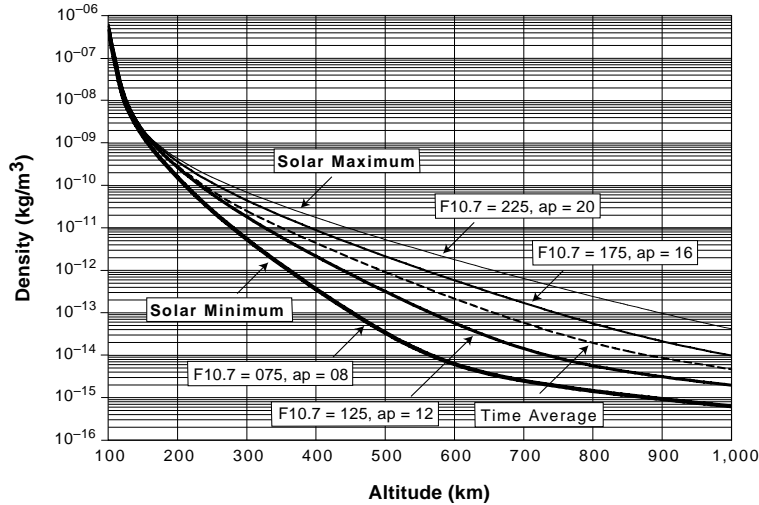
Fig. 8-2.   **Density vs. Altitude for Various F10.7 Values.** Note that the curves have the same shape as the altitude maintenance curves in Fig. 7-8**.**
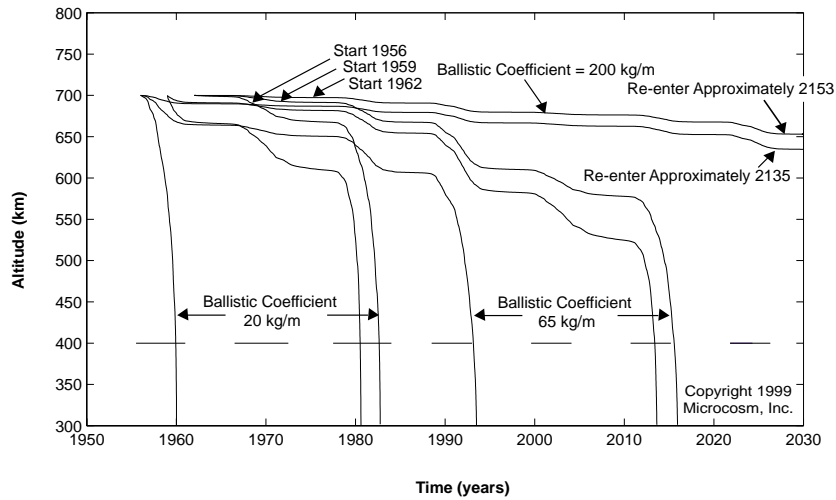
Fig. 8-3.   **Altitude as a Function of Date for 9 Hypothetical Satellites Launched over a 6-Year Period.** The bars at approximately 400 km altitude mark the periods of solar maxima when the Fl0.7 index was above 150.

more slowly. Note that the time for satellite decay is generally measured better in solar cycles than in years. All 9 satellites reentered during periods of solar maximum. For the range of ballistic coefficients shown, the lifetimes varied from approximately half of a solar cycle (5 years) to 17 solar cycles (190 years). Predicting where the satellite would come down would be remarkably difficult.

The factor *K* should be 2 when *R* is less than 0.5, and 1 otherwise. This reflects an additional factor of 2 in weight and power for increased margin when scaling the system down by a factor of more than 2. When the system grows, the R^3 term will directly add a level of margin. For instruments more than a factor of five smaller than those listed in Table 9-13, scaling becomes unreliable. We recommend assuming a mass density of 1 gm/cm^3 and power density of 0.005 W/cm^3 for small instruments. An example of these computations for FireSat is in Sec. 9.6.1.

9.5.4 Evaluate Candidate Payloads

Multi-attribute performance indices can be defined for comparing optical instruments with similar performance characteristics. For high-resolution spatial instruments three basic values describe the quality (corresponding to the information content) in the image. The three defining features are the signal-to-noise ratio at spatial frequency zero (high SNR corresponds to high information content), the MTF of an instrument at the Nyquist frequency (high MTF corresponds to high information content for sampling rates between zero and the Nyquist frequency), and the ground sample distance GSD (small GSD corresponds to high information content). We define a *relative quality index* (RQI) to allow straightforward quantitative comparisons with a reference instrument denoted by the suffix ref.

$$RQI = \frac{SNR}{SNR_{ref}} \frac{MTF}{MTF_{ref}} \frac{GSD_{ref}}{GSD} \qquad (9\text{-}22)$$

This relative quality index allows the designer to trade requirements with respect to each other. For example, a higher SNR can compensate for a lower MTF at the Nyquist frequency for a given GSD. Such comparisons allow for first-order insights into the relationships between complexity, performance, and cost of candidate sensors. For example, suppose we define a reference instrument to have an SNR of 512, and an MTF of 0.5 and a GSD of 25 m. If we then compute design parameters for a particular mission, we can generate a relative quality index, or score, for our design with respect to the reference instrument. For instance, if our design choices lead us to an instrument with a SNR of 705.2, a MTF of 0.47 and a GSD of 30 m, then the RQI for this system will be 108%. This index offers a straightforward method for comparing several competing sensors across three key performance measures.

9.5.5 Observation Payload Design Process

Table 9-15 contains the details of the design process for visible and infrared systems. We begin with basic design parameters such as the orbital height, minimum observation angle and ground resolution. We then compute the quantities that describe the performance of the instrument. In particular, we determine the pixel processing parameters and system data rate, the size of the optics for a given pixel size, and the radiometry of the sensor. Sample computations for the FireSat payload are given in the third column.

The data rate required for observation payloads depends on the resolution, coverage, and amplitude accuracy. With the maximum look angle, η, spacecraft altitude, *h*, and cross-track pixel size, *X*, we have to image $2\eta h / X$ pixels per swath line (cross-track). With the spacecraft ground-track velocity V_g and the along-track pixel size *Y* we have to scan V_g / Y swath lines in one second. If we quantify the intensity of each pixel by *b* bits (2^b amplitude levels) we generate a data rate, *DR*, of

$$DR = \frac{2\eta h}{X} \cdot \frac{V_g}{Y} \cdot b \approx \frac{S_w}{X} \cdot \frac{V_g}{Y} \cdot b \qquad \text{bits/second (bps)} \qquad (9\text{-}23)$$

where η is the maximum look angle in radians, h is the orbit altitude, V_g is the space-craft ground-track velocity, S_w is the swath width, X is the across-track pixel dimension, and Y is the along-track pixel dimension. The approximation is good for small swath widths. The data rate can be increased by transmission overhead such as house-keeping data or coding and it can be decreased by data compression. (See Secs. 2.1.1, 13.2.2, and 15.3.2.).

TABLE 9-15. Calculation Design Parameters for a Passive Optical Sensor.

Step	Calculation	FireSat	Comments
Step 1. Define Orbit Parameters			
Define orbital altitude, h	Design parameter†	$h = 700$ km	See Table 3-4, Sec. 7.4
Compute orbit period, P	Eq. (7-7), IRC*	$P = 98.8$ min	Assumes circular orbit
Compute ground track velocity, V_g	Eq. (5-31), IRC*	$V_g = 6.76$ km/s	Assumes circular orbit
Compute node shift, ΔL	Eq. (7-13), IRC*	$\Delta L = 24.8$ deg	Function of inclination
Step 2. Define Sensor Viewing Parameters			
Compute angular radius of the Earth, ρ	Eq. (5-15), IRC*	$\rho = 64.3$ deg	Depends on orbital altitude
Compute max. distance to the horizon, D_{max}	Eq. (5-17), IRC*	$D_{max} = 3,069$ km	Depends on orbital altitude
Define max. incidence ang. IA, or max. Earth cen. ang. ECA_{max}	Design parameter, IRC*	$IA = 70$ deg	Adjust swath width for good coverage (Sec. 7.4)
Compute sensor look angle (= nadir angle), η	Eqs. (5-24) or (5-25b), IRC*	$\eta = 57.9$ deg	Will be less than ρ
Compute min. elev. angle, $\varepsilon = 90° - IA$	Eqs. (5-25b) and (5-26), IRC*	$\varepsilon = 20$ deg	If max. ECA_{max} given, compute ε
Compute max. Earth central angle, ECA_{max}	Eqs. (5-25b) and (5-26), IRC*	$ECA_{max} = 12.1$ deg	If ε given, compute ECA_{max}
Compute slant range, R_S	Eq. (5-27), IRC*	$R_S = 1,578$ km	R_S here = D in Chap. 5
Find swath width	$= 2\,ECA_{max}$	$2\,ECA_{max} = 24.2$ deg	Determines coverage
Step 3. Define Pixel Parameters and Data Rate			
Specify max. along-track ground sampling dist., Y_{max}	Design parameter	$Y_{max} = 68$ m	Based on spatial resolution requirements at ECA_{max}
Determine instantaneous field of view, $IFOV$	$IFOV = \frac{Y_{max}}{R_S} \cdot \frac{180 \text{ deg}}{\pi}$	$IFOV = 0.00245$ deg	One pixel width
Find max. cross-track pixel resolution, X_{max}, at ECA_{max}	$X_{max} = \frac{Y_{max}}{\cos(IA)}$	$X_{max} = 199.6$ m	Driven by resolution requirement at maximum slant range

* IRC = parameter tabulated on the Inside Rear Cover for Earth Satellites Parameters.
†Calculations are based on a circular orbit.

must analyze a number of worst hot, cold, and maximum gradient cases which we pass to the structural engineer.

- *Thermal Mathematical Model Correlation*—With this process we reduce the errors affecting the temperature predictions when thermal-test results are available. We do this by comparing the predicted and measured average temperatures, at convenient locations, during testing. Typically, if they differ more than 3°C, then we must increase the realism/accuracy of the thermal model.

- *Subsystem Budgets Preparation*—We request the thermal subsystem designers to establish a budget for each of the following resources: mass, size, power, energy, telemetry and telecommand channels, all along the TCS life cycle. We use these budgets to control the status of the thermal design, to provide inputs to other subsystems, and to discuss with the system authority.

Trade Studies—In this section we have described many of the hardware elements of a thermal control system. The question remains, which hardware elements should we use, or even consider, for a given spacecraft? We often answer this question in practice by performing trade studies to determine the most effective components to use for a given situation. The criteria used in trade studies usually involves: thermal performance, cost, weight, reliability, design flexibility, accessibility, testability, availability, safety, and durability. During the spacecraft design phase, a concurrent engineering approach should be applied; i.e. the thermal design should be developed in parallel with the overall spacecraft and mission design and not sequentially in order to establish the most efficient TCS concept in terms of time and money.

11.5.7 Thermal Testing

We perform thermal tests at both component, subsystem and system levels to verify the thermal design and demonstrate the proper operation of items in extreme environmental conditions. The following definitions apply to spacecraft and spacecraft components thermal testing.

Figure 11-24 makes clear the following temperature definitions.

Predicted Temperature Range—It's a temperature range defined by the minimum and maximum temperatures predicted from a thermal analysis considering conservative parameters. This means to consider undegraded thermo-optical properties, no or minimum power dissipation and environmental thermal fluxes for cold cases, and degraded thermo-optical properties and maximum power dissipation and environmental thermal fluxes for hot cases.

Design Temperature Range—(Sometimes called operating or expected temperatures). It's a temperature range defined by the predicted extreme temperatures plus thermal uncertainties. *Thermal uncertainties* traditionally range from 5 °C to 7 °C for a final analysis campaign after model correlation, to 10 °C for design definition analyses, to 15 °C for preliminary design definition analysis. They are introduced to compensate for the inevitable uncertainties due to inaccuracies in modeling, knowledge of environmental parameters, and thermal hardware characteristics. Thermal uncertainties are analogous to factor of safety in structural design. The design temperature range can either be the requirement for the termal designer or the result of his analysis.

Acceptance Temperature Range—It's specified for the operating and non-operating modes of a unit and defined by the design extreme temperature range with a
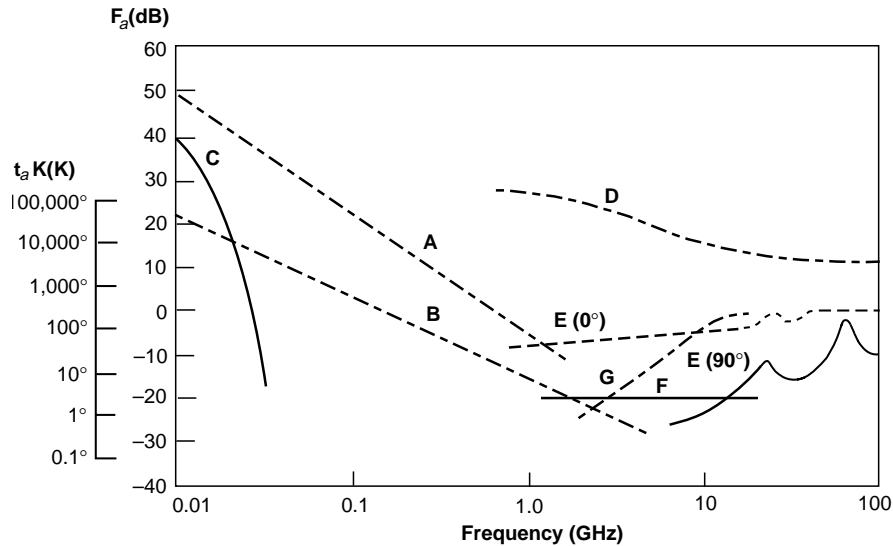
A: Estimated median business area man-made noise
B: Galactic noise
C: Atmospheric noise, value exceeded 0.5% of time
D: Quiet Sun (1/2 deg beamwidth directed at Sun)
E: Sky noise due to oxygen and water vapor (very narrow beam antenna);
   upper curve, 0-deg elevation angle; lower curve, 90-deg elevation angle
F: Black body (cosmic background), 2.7 K
G: Heavy rain (50 mm/hr over 5 km)

Fig. 13-7. Minimum Expected External Noise From Natural and Man-made Sources, 10 MHz to 100 GHz [Ippolito, 1986].

All noise sources between the antenna terminal and the receiver output are lumped together and called *receiver noise temperature, T_r*. Receiver noise originates from

- *Transmission Lines and Filters*—equal to $(1 - L)T$, where $L \equiv P_o / P_i$ is the ratio of output power (P_o) to input power (P_i) and T is the component temperature in K.

- *Low Noise Amplifier*—equal to $(F - 1)$ 290 K, where F is the noise figure from Eq. (13-24).

An additional contribution from subsequent amplifier stage noise exists, but is a small contributor because it is divided by the low noise amplifier gain.

The *noise figure*, F, of the receiver is defined as:

$$F = 1 + \frac{T_r}{T_0} \tag{13-24}$$

where T_r is the noise temperature of the receiver itself, and T_0 is a reference temperature, usually 290 K. The noise figure is often expressed in dB (that is, 10 log F). For example, a cryogenically cooled receiver for reception of telemetry signals from a space probe may have a noise figure of 1.1 (0.4 dB) for a noise temperature of 29 K.

13.3.6 Link Budgets

The link budget provides the designer with values of transmitter power and antenna gains for the various links in the system. It is therefore one of the key items in a space system design, revealing many characteristics of the overall system performance. Table 13-13 presents link budgets for FireSat command and telemetry using the equations and figures given in this chapter.

TABLE 13-13. Link Budgets for FireSat.

Item	Symbol	Units	Source	Command	Telemetry and Data
Frequency	f	GHz	Input parameter	2	2.2
Transmitter Power	P	Watts	Input parameter	1	20
Transmitter Power	P	dBW	$10\log(P)$	0.0	13.0
Transmitter Line Loss	L_l	dB	Input parameter	−1	−1
Transmit Antenna Beamwidth	θ_t	deg	Input parameter	2.0	32.0
Peak Transmit Antenna Gain	G_{pt}	dBi	Eq. (13-20)	38.3	14.2
Transmit Antenna Diameter	D_t	m	Eq. (13-19)	5.3	0.3
Transmit Antenna Pointing Offset	e_t	deg	Input parameter	0.2	27
Transmit Antenna Pointing Loss	L_{pt}	dB	Eq. (13-21)	−0.1	−8.5
Transmit Antenna Gain (net)	G_t	dBi	$G_{pt} + L_{pt}$	38.2	−5.7
Equiv. Isotropic Radiated Power	EIRP	dBW	$P + L_l + G_t$	37.2	17.7
Propagation Path Length	S	km	Input parameter	2,831	2,831
Space Loss	L_s	dB	Eq. (13-23a)	−167.5	−168.3
Propagation & Polarization Loss	L_a	dB	Fig. 13-10	−0.3	−0.3
Receive Antenna Diameter	D_r	m	Input parameter	0.07	5.3
Peak Receive Antenna Gain (net)	G_{rp}	dBi	Eq. (13-18a)	0.74	39.1
Receive Antenna Beamwidth	θ_r	deg	Eq. (13-19)	150.0	1.8
Receive Antenna Pointing Error	e_r	deg	Input parameter	70	0.2
Receive Antenna Pointing Loss	L_{pr}	dB	Eq. (13-21)	−2.6	−0.1
Receive Antenna Gain	G_r	dBi	$G_{rp} + L_{pr}$	−1.9	39.0
System Noise Temperature	T_s	K	Table 13-10	614	135
Data Rate	R	bps	Input parameter	100	85×10^6
E_b/N_o (1)	E_b/N_o	dB	Eq. (13-13)	45.5	15.9
Carrier-to-Noise Density Ratio	C/N_o	dB-Hz	Eq. (13-15a)	65.5	95.2
Bit Error Rate	BER	—	Input parameter	10^{-7}	10^{-5}
Required E_b/N_o (2)	Req E_b/N_o	dB	Fig. 13-9	11.3	9.6
Implementation Loss (3)	—	dB	Estimate	−2	−2
Margin	—	dB	(1) − (2) + (3)	32.2	4.3

Technique	Time	Frequency	Advantages	Disadvantages
Frequency Division Multiple Access (FDMA)			• Continuous carrier transmission. • Peak and average power equal. • No complex timing. • Modulation rates comparable to user data rates. • Inexpensive ground stations.	• Multiple users cannot share single transmitter without mutual interference or low power efficiency. • Requires complex filter banks to separate channels. • Difficult filtering to separate large power users from adjacent users. • May require power control.
Time Division Multiple Access (TDMA)			• Multiple users can share single transmitters with high efficiency. • Simple timing logic easily separates large numbers of individual users. • Compatible with beam-hopped satellite antenna. • Can handle large power variations between users.	• Pulsed carrier transmission makes peak power greater than average. • Requires precise time synchronization. • Modulation burst rates high compared to user data rates. • Requires memory buffers.
Code Division Multiple Access (CDMA)			• Relatively immune to transmitter distortion, multipath and interference. • Inherent privacy.	• Limited to low data rates relative to transmission boundaries. • Limited number of users due to mutual interference. • Limited variation in power differences between users. • Needs precise time synchronization.

Fig. 13-16.   Multiple Access Techniques Allow Different Users to Share the Same Transmission Channel.

(Fig. 13-17D). The PN code modulation is completely removed, leaving the desired user signal "despread." At the same time, the signals from the undesired users appear at the output of the mixer as PN-coded signals with a spectrum width roughly twice the PN-code rate. Therefore, only a small portion of the undesired signal will pass through the narrow-band output BPF.

TABLE 16-17. Commercially Available Space Computers. These computers have been developed for use in a variety of general purpose space applications.

Supplier and Computer	ISA	Word Length (bits)	Memory (RAM + EEPROM)	Perfor-mance (MIPS)	Radiation Hardness	Connect-ivity	Heritage
Honeywell GVSC	1750A	16	16 MB*	1 to 3	1 MRad	1553B RS-232 RS-422	NEAR, ChinaStar, Clementine
Honeywell RH32	R 3000	32	4 GB	10 to 20	1 MRad	1553B RS-232 RS-422	GPS II SBIRS High
Honeywell RHPPC	603E	32	4 GB	20	100 KRad	RS-232 RS-422	VIIRS
L-M GVSC	1750A	16	16 MB*	1 to 2	1 MRad	1553B RS-232 IEEE-488	Cassini, Rapid I
L-M RAD 3000	R 3000	32	16 MB	10	Rad Hard	1553B RS-422	LM-900
L-M RAD 6000	RS 6000	32	16 GB	10 to 20	100 KRad	PCI Firewire HSS	Mars Pathfinder, Global-star, Space Station, SBIRS Low, Mars 98
TRW	RS-3000	32	16 MB	10	Rad Hard	1553B RS-422	SSTI, T200b, Step-E
SWRI SC-2A	80C186	16	768 KB	0.3	10 KRad	Parallel RS-422	MSTI-2
SWRI SC-5	80C386	32	320 KB	0.6	10 KRad	Parallel RS-422	RADARSAT, SNOE
SWRI SC-7	TI320C30	32	640 KW	12	100 KRad	1553B	MSTI-3
SWRI SC-1750A	1750A	16	512 KB	1	10 KRad	RS-422 1553B	MSTI-1,2,3 New Millennium DS-1
SWRI SC-9	RS 6000	32	128 MB	20	30 KRad	RS-232	Space Station
SWRI MOPS	R 6000	32	128 MB	25	30 KRad	RS-422	Gravity Probe B, International Space Station Alpha (ISSA)
Sanders STAR-RH	R 3000	32	4 MB	10	50 KRad	1553B	CRSS
GDAIS ISE	603E	32	2 GB	25	Rad Hard	1553B	HEAO, AFAX
Acer Sertek	80186	16	512 KB	0.5	Rad Hard	1553B RS-422	ROCSAT

* Address Space   L-M: Lockheed Martin   SWRI: Southwest Research Institute

For example, a computer with 16 bit words would generally have a 64K word address space and a 32 bit word computer could address a 4 Gigaword address space. However, this may require a more in-depth examination. The Generic VHSIC Spaceborne Computer (GVSC) was developed by the Air Force from the MIL-STD 1750A, which defines one word as 16 bits, but it has an 8 Mword address space. This was achieved by built-in paging hardware. The GVSC is a special case because the Air Force developed it especially for space applications. We may find other exceptions as well.

If possible each candidate computer, or its engineering development unit equivalent, should be bench-marked against the relevant applications. This is rarely done because of time and lack of availability of the hardware. In the absence of real equipment or software benchmarks, the computer analyst should examine the individual instructions of each candidate and match them against the qualitative aspects of the computational requirements. For example, the processor we select to support the attitude determination and control function will perform many floating point and transcendental function computations. In this case it would be desirable for floating point and trigonometric instructions to be performed in hardware and not in software.

TABLE 17-9.   Electric Propulsion; Three Classes of Accelerator Concepts.

	Electrothermal	Electrostatic	Electromagnetic
Mechanism	• Gas heated via resistance element or arc and expanded through nozzle • Resistojets • Arcjets	• Ions electrostatically accelerated • Hall effect (HET) • Ion • Field emission	• Plasma accelerated via interaction of current and magnetic field • Pulsed plasma (PPTs) • Magnetoplasmadynamic (MPD) • Pulsed inductive (PIT)
Power	0.4–2 kW	1–50 kW	50 kW–1 MW
Specific Impulse, I_{sp}	300–800 sec	1,000–3,000 sec	2,000–5,000 sec

TABLE 17-10.   Characteristics of Selected Electric Propulsion Flight Systems.

| Concept	Specific Impulse, (sec)	Input Power, (kW)	Thrust/ Power, (mN/kW)	Specific Mass, (kg/kW)	Propellant	Supplier
Resistojet	296	0.5	743	1.6	N_2H_4	Primex
	299	0.9	905	1	N_2H_4	Primex, TRW
Arcjet	480	0.85	135	3.5	NH_3	IRS/ITT
	502	1.8	138	3.1	N_2H_4	Primex
	>580	2.17	113	2.5	N_2H_4	Primex
	800	26[*]	—	—	NH_3	TRW, Primex, CTA
Pulsed Plasma Thruster (PPT)	847	< 0.03[†]	20.8	195	Teflon	JHU/APL
	1,200	< 0.02[†]	16.1	85	Teflon	Primex, TSNIIMASH, NASA
Hall Effect Thruster (HET)	1,600	1.5	55	7	Xenon	IST, Loral, Fakel
	1,638	1.4[*]	—	—	Xenon	TSNIIMASH, NASA
	2,042	4.5	54.3	6	Xenon	SPI, KeRC
Ion Thruster (IT)	2,585	0.5	35.6	23.6	Xenon	HAC
	2,906	0.74	37.3	22	Xenon	MELCO, Toshiba
	3,250	0.6	30	25	Xenon	MMS
	3,280	2.5	41	9.1	Xenon	HAC, NASA
	3,400	0.6	25.6	23.7	Xenon	DASA

* Thruster input power.
† Power dependent on pulse rate.

developed by Primex. Resistojets have several desirable features including values of thrust/power far higher than other EP options (due to their high efficiencies and modest specific impulses), the lowest EP system dry masses (primarily due to the lack of a requirement for a power processor), and uncharged/benign plumes. These features will continue to make resistojets attractive for low-to-modest energy applications, especially where power limits and/or thrusting times, and/or plume impacts are mission drivers. In addition, resistojets can operate on a wide variety of propellants which led to their proposed use as a propulsion/waste gas management concept on Space Station and, operated on hydrogen, for Earth-orbit insertions.

can effectively shield against. Thus, there are a significant number of objects that we cannot track, but which can cause substantial spacecraft damage.

We can quantify how crowded space has become by using the *spatial density,* i.e., the number of objects per volume of space. Figure 21-3 plots spatial density values out to 2,000 km altitude for cataloged objects of various sizes. The GEO curve represents the spatial density within 1 deg of the equatorial plane. The average density between 800 and 1,000 km is just above 10^{-8} km^{-3}. The smallest trackable objects may weigh tens to hundreds of grams. We cannot shield against objects of this size. In GEO the average spatial density is one to two orders of magnitude less than LEO. The **average** relative velocity in LEO between orbiting objects is 9 to 10 km/s with maximum values above 14 km/s due to eccentric and retrograde orbits. In comparison, the relative velocity between debris and satellites in GEO ranges between 100 and 500 m/s. The difference in relative velocities is due mainly to the lower orbital velocities and smaller inclination distribution of objects in GEO. This physical phenomenon couples with the lower spatial density values in GEO to make the collision hazard much smaller in GEO than LEO.
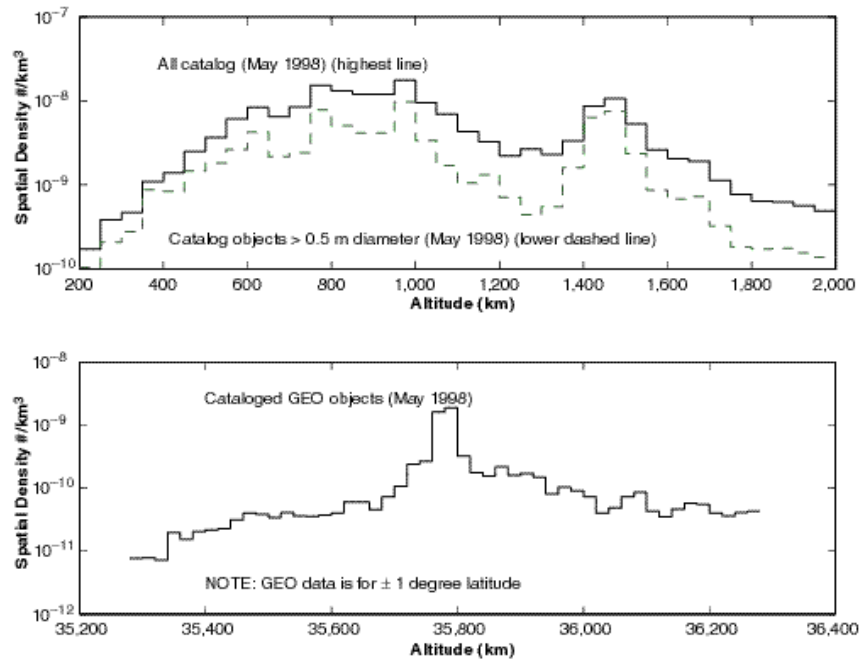
Fig. 21-3.   Spatial Density Values. Densities in GEO are approximately 10 times less than in LEO. The probability of a spacecraft getting hit by something big is small, while the chance of getting hit by something small is big. See text for discussion.

In addition to the spatial density being different in LEO vs. GEO, the natural cleansing effects also differ. In GEO and geosynchronous transfer orbit the major perturbations are solar/lunar gravitational effects. For very small debris, solar radiation pressure may also significantly affect lifetimes. Atmospheric drag at GEO has no

Appendix E
Universal Time and Julian Dates

James R. Wertz, *Microcosm, Inc.*

Calendar time in the usual form of date and time is used only for input and output because arithmetic is cumbersome in months, days, hours, minutes, and seconds. Nonetheless, this is used for most human interaction with space systems because it's the system with which we are most familiar. Even with date and time systems, problems can arise, because time zones are different throughout the world and spacecraft operations typically involve a worldwide network. The uniformly adopted solution to this problem is to use the local standard time corresponding to 0 deg longitude (i.e., the Greenwich meridian) as the assigned time for events anywhere in the world or in space. This is referred to as *Universal Time* (UT), *Greenwich Mean Time* (GMT), or *Zulu* (Z), all of which are equivalent for most practical spacecraft operations. The name Greenwich Mean Time is used because 0 deg longitude is defined by the site of the former Royal Greenwich Observatory in metropolitan London.

Civil time, T_{civil}, as measured by a standard wall clock or time signals, differs from Universal Time by an integral number of hours, corresponding approximately to the longitude of the observer. The approximate relation is:

$$T_{civil} \approx UT \pm (L + 7.5)/15 \qquad \text{(E-1)}$$

where T_{civil} and UT are in hours, and L is the longitude in degrees with the plus sign corresponding to East longitude and the minus sign corresponding to West longitude. The conversion between civil time and Universal Time for most North American and European time zones is given in Table E-1. Substantial variations in time zones are created for political convenience. In addition, most of the United States and Canada observe Daylight Savings Time from the first Sunday in April until the last Sunday in October. Most European countries observe daylight savings time (called "summer time") from the last Sunday in March to the first Sunday in October. Many countries in the southern hemisphere also maintain daylight savings time, typically from October to March. Countries near the equator typically do not deviate from standard time.

Calendar time is remarkably inconvenient for computation, particularly over long time intervals of months or years. We need an absolute time that is a continuous count of time units from some arbitrary reference. The time interval between any two events may then be found by simply subtracting the absolute time of the second event from that of the first. The universally adopted solution for astronomical problems is the *Julian Day*, JD, a continuous count of the number of days since Greenwich noon (12:00 UT) on January 1, 4713 BC*, or, as astronomers now say, –4712. Because Julian Days start at noon UT, they will be a half day off with respect to civil dates. While this is inconvenient for transforming from civil dates to Julian dates, it was useful for astronomers because the date didn't change in the middle of the night (for European observers).

TABLE E-1.   Time Zones in North America, Europe, and Japan. In most of the United States, Daylight Savings Time is used from the first Sunday in April until the last Sunday in October. In Europe, the equivalent "summer time" is used from the last Sunday in March to the first Sunday in October.

Time Zone	Standard Meridian (Deg, East Long.)	UT Minus Standard Time (Hours)	UT Minus Daylight Time (Hours)
Atlantic	300	4	3
Eastern	285	5	4
Central	270	6	5
Mountain	255	7	6
Pacific	240	8	7
Alaska	225	9	8
Hawaii	210	10	NA
Japan	135	−9	NA
Central Europe	15	−1	−2
United Kingdom	0	0	−1

As described below, there are four general approaches for converting between calendar dates and Julian dates.

Table Look-Up

Tabulations of the current Julian Date are in most astronomical ephemerides and almanacs. Table E–2 lists the Julian Dates at the beginning of each year from 1990 through 2031. To find the Julian Date for any given calendar date, simply add the *day number* within the year (and fractional day number, if appropriate) to the Julian Date for Jan 0.0 of that year from Table E–2. Day numbers for each day of the year are on many calendars or can be found by adding the date to the day number for day 0 of the month from Table E-3. Thus 18:00 UT on April 15, 2002 = day number 15.75 + 90 = 105.75 in 2002 = JD 105.75 + 2,452,274.5 = JD 2,452,380.25.

To convert from Julian Days to dates, determine the year in which the Julian Date falls from Table E–2. Subtract the Julian Date from the JD for January 0.0 of that year to determine the day number within the year. This can be converted to a date (and time, if appropriate) by using day numbers on a calendar or subtracting from the day number for the beginning of the appropriate month from Table E–3. Thus, from Table E–2, JD 2,451,608.25 is in the year 2000. The day number is 2,451,608.25 – 2,451,543.5 = 64.75. From Table E–3, this is 18:00 UT, March 4, 2000.

Software Routines Using Integer Arithmetic

A particularly clever procedure for finding the Julian Date, JD, associated with any current year, Y, month, M, and day of the month, D, is given by Fliegel and Van

---

* This strange starting point was suggested by an Italian scholar of Greek and Hebrew, Joseph Scaliger, in 1582 as the beginning of the current *Julian period* of 7,980 years. This period is the product of three numbers: the *solar cycle*, or the interval at which all dates recur on the same days of the week (28 years); the *lunar cycle*, containing an integral number of lunar months (19 years); and the *indiction* or the tax period introduced by the Emperor Constantine in 313 AD (15 years). The last time that these started together was 4713 BC and the next time will be 3267 AD. Scaliger was interested in reducing the astronomical dating problems associated with calendar reforms of his time and his proposal had the convenient selling point that it pre-dated the ecclesiastically approved date of creation, October 4, 4004 BC.

TABLE E–2. Julian Date at the Beginning of Each Year from 1990 to 2031. See text for explanation of use. The day number for the beginning of the year is called "Jan. 0.0" (actually Dec. 31st of the preceding year) so that day numbers can be found by simply using dates. Thus, Jan. 1 is day number 1 and has a JD 1 greater than that for Jan. 0. * = leap year.

Year	*JD* 2,400,000+ for Jan 0.0 *UT*	Year	*JD* 2,400,000+ for Jan 0.0 *UT*	Year	*JD* 2,400,000+ for Jan 0.0 *UT*
1990	47,891.5	2004*	53,004.5	2018	58,118.5
1991	48,256.5	2005	53,370.5	2019	58,483.5
1992*	48,621.5	2006	53,735.5	2020*	58,848.5
1993	48,987.5	2007	54,100.5	2021	59,214.5
1994	49.352.5	2008*	54,465.5	2022	59,579.5
1995	49,717.5	2009	54,831.5	2023	59,944.5
1996*	50,082.5	2010	55,196.5	2024*	60,309.5
1997	50,448.5	2011	55,561.5	2025	60,675.5
1998	50,813.5	2012*	55,926.5	2026	61,040.5
1999	51,178.5	2013	56,292.5	2027	61,405.5
2000*	51,543.5	2014	56,657.5	2028*	61,770.5
2001	51,909.5	2015	57,022.5	2029	62,136.5
2002	52,274.5	2016*	57,387.5	2030	62,501.5
2003	52,639.5	2017	57,753.5	2031	62,866.5

TABLE E–3. Day Numbers for Day 0.0 of Each Month. Leap years (in which February has 29 days) are those evenly divisible by 4. However, years evenly divisible by 100 are not leap years, except that those evenly divisible by 400 are. Leap years are indicated by * in Table E–2.

Month	Non-Leap Years	Leap Years
January	0	0
February	31	31
March	59	60
April	90	91
May	120	121
June	151	152
July	181	182
August	212	213
September	243	244
October	273	274
November	304	305
December	334	335

Flandern [1968] as a computer statement using integer arithmetic. Note that all of the variables must be defined as integers (i.e., any remainder after a division must be truncated) and that both the order of the computations and the parentheses are critical. This procedure works in FORTRAN, C, C++, and Ada for any date on the Gregorian calendar that yields JD > 0. (Add 10 days to the JD for dates on the Julian calendar prior to 1582.)

$$JD_0 = D - 32{,}075 + 1461 \times (Y + 4800 + (M - 14)/12)/4$$
$$+ 367 \times (M - 2 - (M - 14)/12 \times 12)/12$$
$$-3 \times ((Y + 4900 + (M - 14) / 12) / 100) /4 \qquad \text{(E-2a)}$$

Here JD_0 is the Julian Day beginning at noon UT on the given date and must be an integer. For a fractional day, F, in UT (i.e., day number D.F), the floating point Julian Day is given by:

$$JD = JD_0 + F - 0.5 \qquad \text{(E-2b)}$$

For example, the Julian Day beginning at 12:00 UT on December 25, 2007 (Y = 2007, M = 12, D = 25) is JD 2,454,460 and 6:00 UT on that date (F = 0.25) is JD 2,454,459.75.

The inverse routine for computing the date from the Julian Day is given by:

$$L = JD_0 + 68{,}569 \qquad \text{(E-3a)}$$

$$N = (4 \times L) / 146{,}097 \qquad \text{(E-3b)}$$

$$L = L - (146097 \times N + 3) / 4 \qquad \text{(E-3c)}$$

$$I = (4000 \times (L + 1)) / 1{,}461{,}001 \qquad \text{(E-3d)}$$

$$L = L - (1461 \times I) / 4 + 31 \qquad \text{(E-3e)}$$

$$J = (80 \times L) / 2{,}447 \qquad \text{(E-3f)}$$

$$D = L - (2447 \times J) / 80 \qquad \text{(E-3g)}$$

$$L = J / 11 \qquad \text{(E-3h)}$$

$$M = J + 2 - 12 \times L \qquad \text{(E-3i)}$$

$$Y = 100 \times (N - 49) + I + L \qquad \text{(E-3j)}$$

where integer arithmetic is used throughout. Y, M, and D are the year, month, and day, and I, J, L, and N are intermediate variables. Finally, again using integer arithmetic, the day of the week, W, corresponding to the Julian Date beginning at 12:00 on that day is given by:

$$W = JD_0 - 7 \times ((JD + 1) / 7) + 2 \qquad \text{(E-4)}$$

where W = 1 corresponds to Sunday. Thus, December 25, 2007 falls on Tuesday.

Software Routines Without Integer Arithmetic

While most computer languages provide integer arithmetic, spreadsheets such as Excel or MatLab typically do not. (See below for use of Excel and MatLab DATE functions.) Similar capabilities are available using integer (INT) or truncation (TRUNC in Excel, FIX in MatLab) functions. INT and TRUNC are identical for positive numbers, but differ for negative numbers: INT(–3.1) = –4, whereas

TRUNC(–3.1) = –3. It is the TRUNC or FIX function which is equivalent to integer arithmetic. Thus, using the same variables as above, we can rewrite Eqs. (E-2) for computation of JD from the date as:

$$C = TRUNC((M - 14)/12) \tag{E-5a}$$

$$\begin{aligned} JD_0 = D &- 32{,}075 + TRUNC(1{,}461 \times (Y + 4{,}800 + C)/4) \\ &+ TRUNC(367 \times (M - 2 - C \times 12)/12) \\ &- TRUNC(3 \times (TRUNC(Y + 4{,}900 + C) / 100) / 4) \end{aligned} \tag{E-5b}$$

$$JD = JD_0 + F - 0.5 \tag{E-5c}$$

where again JD_0, Y, M, D, and C are integers and F and JD are real numbers. Applying the same rules to Eq. (E-3) gives the inverse formula for the date in terms of JD as:

$$L = JD + 68{,}569 \tag{E-6a}$$

$$N = TRUNC((4 \times L) / 146{,}097) \tag{E-6b}$$

$$L = L - TRUNC((146097 \times N + 3) / 4) \tag{E-6c}$$

$$I = TRUNC((4000 \times (L + 1)) / 1{,}461{,}001) \tag{E-6d}$$

$$L = L - TRUNC((1{,}461 \times I) / 4) + 31 \tag{E-6e}$$

$$J = TRUNC((80 \times L) / 2{,}447) \tag{E-6f}$$

$$D = L - TRUNC((2{,}447 \times J) / 80) \tag{E-6g}$$

$$L = TRUNC(J / 11) \tag{E-6h}$$

$$M = J + 2 - 12 \times L \tag{E-6i}$$

$$Y = 100 \times (N - 49) + I + L \tag{E-6j}$$

where the variables are the same as Eq. (E-3), except that D is now a real number corresponding to the date and fraction of a day. Finally, Eq. (E-4) for the day of the week becomes:

$$\begin{aligned} W &= JD - 7 \times TRUNC((JD + 1.5) / 7) + 2.5 \\ &= JD - 7 \times INT((JD + 1.5) / 7) + 2.5 \end{aligned} \tag{E-7}$$

where $1 \le W < 2$ corresponds to Sunday. The examples given above can also serve as test cases for Eqs. (E-5), (E-6), and (E-7).

Modified Julian Date

The Julian Date presents minor problems for space applications. Because it was introduced principally for astronomical use, Julian Dates begin at 12:00 UT rather than 0 hours UT, as the civil calendar does (thus the 0.5 day differences in Table E–2). In addition, the 7 digits required for the Julian Date did not permit the use of single precision arithmetic in older computer programs. This is no longer a problem with modern computer storage and number formats. Nonetheless, various forms of truncated Julian dates have gained at least some use.

The most common of the truncated Julian dates for astronomical and astronautics use is the *Modified Julian Date*, MJD, given by:

$$MJD = JD - 2{,}400{,}000.5 \tag{E-8}$$

MJD begins at midnight, to correspond with the civil calendar. Thus, in using

Table E–2, the MJD is given by adding the day of the year (plus fractions of a day, if appropriate) to the number in the table, with the ".5" at the end of the table-listing dropped. For example, the MJD for 18:00 UT on Jan. 3, 2002 = MJD 52,277.75. The definition of the MJD given here is that adopted by the International Astronomical Union in 1997. Note, however, that other definitions of the MJD have been used. Thus, the most unambiguous approach remains the use of the full Julian Date.

Spreadsheets such as Excel or MatLab

Spreadsheets, such as Excel or MatLab, typically store dates internally as some form of day count and allow arithmetic operations, such as subtraction. Thus, we can either subtract two dates directly to determine a time interval or convert them to Julian Dates by simply finding the additive constant, K, given by:

$$K = JD - I \qquad \text{(E-9)}$$

where I is the internal number representing a known date, JD. Once this is determined, then the JD for any date is:

$$JD = K + I \qquad \text{(E-10)}$$

Many versions of Excel use Jan. 1, 1904, as "day 0," such that $K_{Excel} = 2,416,480.5$. However, this should be checked for individual programs because other starting points are sometimes used and the starting point is a variable parameter in some versions of Excel. While this can be a very convenient function, Excel date routines run only from 1904 to 2078.

MatLab typically uses Jan. 1, 0000, 0:0:0 as "day 0." Thus, in the formula above, $K_{MatLab} = 1,721,058.5$.

Any of the day counting approaches will work successfully over its allowed range. However, systems intended for general mathematics or business use may not account correctly for leap years and calendar changes when historical times or times far in the future are being evaluated. Thus, the use of the full Julian Date remains the most unambiguous solution, particularly if a program or result is to be used by more than one person or program. For a more extended discussion of time systems, see for example, Seidelmann [1992] or Wertz [1999].

References

Fliegel, Henry F. and Thomas C. Van Flandern. 1968. "A Machine Algorithm for Processing Calendar Dates." *Communications of the ACM*, vol. II, p. 657.

Seidelmann, P. Kenneth. 1992. *Explanatory Supplement to the Astronomical Almanac.* Mill Valley, CA: University Science Books.

Wertz, James R. 1999. *Spacecraft Orbit and Attitude Systems*, vol. I. Torrance, CA and Dordrecht, The Netherlands: Microcosm, Inc. and Kluwer Academic.